

Shear response of the $\Sigma 9 \langle 110 \rangle \{221\}$ symmetric tilt grain boundary in fcc metals studied by atomistic simulation methods

Liang Wan* and Shaoqing Wang

Shenyang National Laboratory for Materials Science, Institute of Metal Research, Chinese Academy of Sciences, Shenyang 110016, People's Republic of China

(Received 6 June 2010; revised manuscript received 1 November 2010; published 20 December 2010)

The shear response of the $\Sigma 9 \langle 110 \rangle \{221\}$ symmetric tilt grain boundary (GB) in three fcc metals Cu, Al, and Ni has been studied by atomistic simulation methods with the embedded atom method for interatomic potentials and with a bicrystal model. By applying an energy minimization procedure, it was found that there are two optimized structures of this particular GB at zero temperature for all the three metals studied. Shear of bicrystals at room temperature has been studied by the molecular-dynamics simulation method. Various kinds of structure evolution behavior have been found for this GB depending on the shear direction: (1) pure GB sliding; (2) GB atomic shuffling accompanied by lattice dislocation emission from the GB; and (3) GB migration coupled with GB sliding, namely, GB coupling motion. The GB coupling motions can differ in the direction and distance of the GB migration depending on the shear direction. An analysis with the aid of the coincidence site lattice theory indicates that the structure evolution behavior can be attributed to several elementary structure transformations inherent to this particular GB. A pair parameter (λ, κ) is proposed to describe the GB coupling motions.

DOI: [10.1103/PhysRevB.82.214112](https://doi.org/10.1103/PhysRevB.82.214112)

PACS number(s): 61.72.Mm, 68.35.Gy, 68.35.bd, 83.10.Mj

I. INTRODUCTION

Grain boundaries (GBs) are an important aspect of microstructure in polycrystalline materials and play a significant role in determining the mechanical properties of these materials.¹ As the temperature increases, or with reduced grain sizes such as those in nanocrystalline or ultrafine-grained materials, GB-mediated plasticity can become the prevailing strain accommodation processes for polycrystalline materials under mechanical loads.^{2,3} Fundamental knowledge of the shear response of GBs is critical for the comprehensive understanding of the mechanical behavior of polycrystalline materials served in these circumstances.^{1,3,4}

Generally, when a GB experiences a certain shear stress, it can slide by translation of the two abutting grains one another.^{1,4} Previous studies indicate that GB sliding at elevated temperatures can be described as a viscous sliding process.^{4,5} The viscosity was also found to be misorientation dependent.⁵⁻⁹ Although these concepts are well developed¹ and are frequently employed in constitutive modeling of the overall mechanical behavior of bulk polycrystals,^{3,4} the underlying atomistic mechanisms are less well understood.¹⁰ Moreover, it is yet unclear as to what extent the high-temperature mechanical behavior of GBs can be extended to the athermal cases such as that for nanocrystalline or ultrafine-grained materials loaded at ambient or even lower temperatures.³

It is suggested that for GBs with a misorientation angle corresponding to a coincidence site lattice (CSL) orientation, the glide of GB displacement shift complete (DSC) dislocations can carry the sliding processes,¹¹⁻¹⁷ and GB migration can be accompanied as GB sliding proceeds.^{13,16-19} However, the CSL-DSC theory is a crystallographic consideration in essence.^{1,13,20,21} The applicability of the CSL-DSC theory on a specific GB with respect to the bonding of materials, the effect of temperature and various external stress conditions

has not been addressed. To be more specific, the following questions need to be clarified: (i) for a GB with given geometry and in a specific material, can the structure of this GB be described by the CSL theory? (ii) If yes, then to what extent (e.g., in what loading conditions) can the sliding behavior of the GB be described by the GB DSC dislocation mechanism? Or is there any other mechanisms which can account for the GB sliding processes? (iii) Among all the possible GB DSC dislocations predicted by the CSL-DSC theory, which one(s) will be in effect under a specific loading condition, and how it will affect the structure transformation behavior of this GB?

Normally, sufficient amount of GBs with various geometries need to be studied to clarify the above issues. In the present work, we chose the $\Sigma 9 \langle 110 \rangle \{221\}$ symmetric tilt GB in three fcc metals Cu, Al, and Ni for the study. Atomistic simulation methods with the embedded atom method (EAM) interatomic potentials together with a bicrystal model were employed to perform the investigation. An energy minimization procedure was first used to obtain the optimized structures of the GBs. The molecular-dynamics (MD) method was then employed to study the shear response of these GBs. By exerting shear loads with different shear directions parallel to the GB plane, we demonstrate that there are various kinds of structure evolution behavior for this particular GB at room temperature depending on the shear direction. The CSL-DSC theory is then employed to give an interpretation of the structure evolution behavior. Finally a brief discussion of the GB coupling motions is given.

II. MODEL AND COMPUTATIONAL METHOD

The bicrystal model used in this work is illustrated in Fig. 1. Three orientations of bicrystals, C1, C2, and C3, were introduced to facilitate the application of shear strain with different shear directions parallel to the GB plane. For each

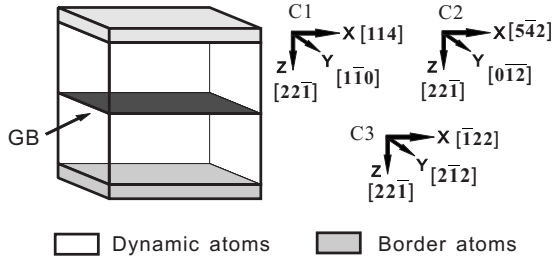


FIG. 1. Geometry of the simulation cell and the bicrystal model used in this work. The three orientations of the bicrystals C1, C2, and C3 are also illustrated. The crystallographic directions are defined with reference to the upper crystal (this convention has been adopted throughout this paper).

orientation, the upper crystal was first constructed with its crystallographic orientation as specified in Fig. 1. The lower crystal was then created by a 180° rotation of the upper crystal around the z axis. The z axis, which is also the normal of the GB plane, is aligned with $[22\bar{1}]$ of the upper crystal. The dimensions of the initial simulation cells used in this work are given in Table I.

Periodic boundary conditions were applied along the x and y directions. A fixed and a damping boundary schemes were used along the z direction for the energy minimization procedure and the MD simulations, respectively. In both the fixed and damping boundary schemes, two slabs along the z axis at the top and bottom of the simulation cell were designed to give the border region (see Fig. 1). The thickness of each slab is slightly larger than the cut-off distance of the interatomic potentials. All the simulations were performed with the LAMMPS code.²²

To obtain the equilibrium structure of the GBs, an energy minimization procedure with a standard conjugate-gradient algorithm was performed on a set of initial trial GB structures. The trial GB structures are distinguished by their in-plane rigid body translation vectors within the GB plane. Since the range of unique in-plane rigid body translation vectors is defined by the cell of nonidentical displacements, which in turn can be related to the unit cell of CSL on the GB plane,¹ a 10×10 grid of points was generated by dividing the unit cell of the CSL on the GB plane to give a uniform sampling of the in-plane translations. Atoms belonging to the border slabs were kept fixed during the energy minimization procedures. The optimized structures obtained were

then subjected to a MD annealing procedure at desired temperatures and zero stress state to ensure their stability.

The shear processes were also simulated by the MD method. An integration time step of 2.0 fs was adopted throughout the MD simulations. Melchionna modified²³ Nosé-Hoover dynamics were applied on atoms between the border slabs for the control of the temperature and stress state of the bicrystals. Atoms belonging to the border slabs cannot move freely. The z -axis component of their coordinates was adjusted uniformly according to the length variation in the simulation cell along this direction. Meanwhile, their motions within the x - y plane were constrained by Langevin dynamics. The damping coefficient in the Langevin dynamics was chosen such that the traverse waves along the z axis can attenuate as quickly as possible. It was found that traverse waves with substantial amplitude can be generated in bicrystals in the occurrence of structure transformations during the shear processes. This damping boundary scheme can effectively eliminate the interference of these waves on the structure transformation behavior of the bicrystals. The stress and temperature were calculated on the dynamic atoms between the two border slabs. The stress tensor was calculated by the standard virial expression.²⁴

Shear strain was applied by deforming the simulation cell as a whole. The shear directions were aligned with the x or y axis of the simulation cell. The stress components in directions other than the shear direction were set to be zero in the Nosé-Hoover dynamics to allow the relaxation of the bicrystals in these directions. Six shear directions parallel to the GB plane were studied: $[1\ 1\ 4]$, $[1\bar{1}0]$, $[5\bar{4}2]$, $[0\bar{1}\bar{2}]$, $[\bar{1}\bar{2}2]$, and $[2\bar{1}2]$. These directions correspond to the positive directions of the x or y axis of the three orientations of the bicrystals as shown in Fig. 1. The shear strain was calculated by measuring the variation in the shape of the simulation cell. A constant strain rate of $1 \times 10^8\ \text{s}^{-1}$ was used for all the straining simulations. The strain rate is several orders higher than that usually used in experiments. This gap is generally due to the intrinsic limit of the MD method employed.

The EAM-type interatomic potentials fitted by Mishin and co-workers for Cu (Ref. 25), Al and Ni (Ref. 26) were used in the atomistic model. These potentials have been well tested and demonstrated to give a good evaluation of a variety of material properties, including the elastic constants, phonon frequencies, thermal expansion, the intrinsic stacking fault energy, the coherent twin boundary energy, etc.^{25,26}

TABLE I. Dimensions of the initial simulation cells used in this work for all the bicrystals studied. C1, C2, and C3 are the three orientations of the bicrystals as illustrated in Fig. 1. N_x , N_y , and N_z represent the number of repeating orthorhombic CSL unit cells inherent to the corresponding orientations of the bicrystals in the x , y , and z directions, respectively. $L_x \times L_y \times L_z$ stands for the actual sizes of the simulation cells. Lattice constants of 3.615 Å, 4.05 Å, and 3.52 Å have been used for Cu, Al, and Ni, respectively. N_{atoms} is the total number of atoms in the bicrystal model.

Orientation	$N_x \times N_y \times N_z$	$(L_x \times L_y \times L_z)_{\text{Cu}}$ (Å ³)	$(L_x \times L_y \times L_z)_{\text{Al}}$ (Å ³)	$(L_x \times L_y \times L_z)_{\text{Ni}}$ (Å ³)	N_{atoms}
C1	$8 \times 19 \times 16$	$122.7 \times 97.1 \times 173.5$	$137.6 \times 108.8 \times 194.4$	$119.5 \times 94.6 \times 169.0$	175104
C2	$5 \times 12 \times 16$	$121.3 \times 97.0 \times 173.5$	$135.8 \times 108.7 \times 194.4$	$118.1 \times 94.5 \times 169.0$	172800
C3	$9 \times 11 \times 16$	$97.6 \times 119.3 \times 173.5$	$109.4 \times 133.7 \times 194.4$	$95.0 \times 116.2 \times 169.0$	171072

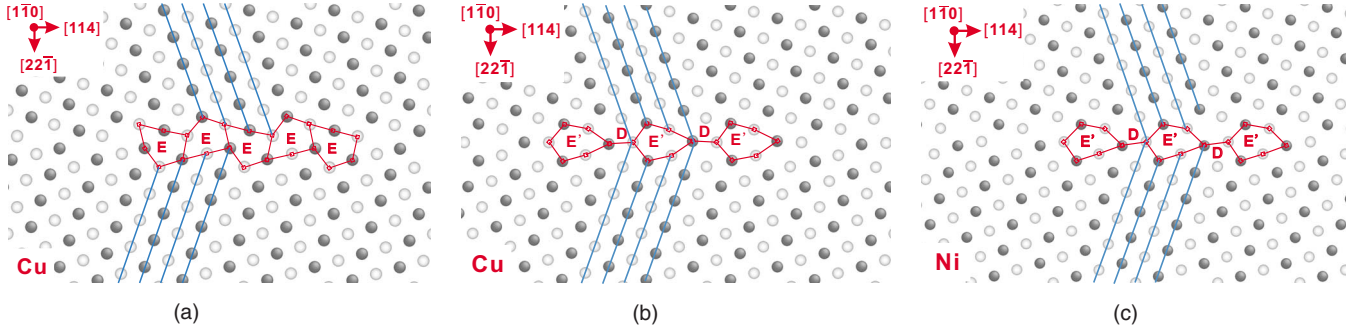


FIG. 2. (Color online) The optimized structures of the $\Sigma 9 \langle 110 \rangle \{ 221 \}$ symmetric tilt GB obtained by the energy minimization procedure and subsequent MD annealing at 300 K and zero stress state. (a) and (b) are the two optimized structures for Cu. (c) is one of the two optimized structures for Ni. Black and white balls correspond to the two alternating $(2\bar{2}0)$ atom layers along the tilt axis $[1\bar{1}0]$. The slashes mark the $\{100\}$ atom layers of the upper and lower crystals. The structural unit sequences of these GBs are also indicated.

The common neighbor analysis (CNA) technique²⁷ was used to identify the defect structures in the bicrystals. This technique gives a classification of all the atoms by their local crystallinity. In our simulation work, three categories of atoms were distinguished: atoms with fcc structural order, atoms with hcp structural order, and atoms with other structural order. Within this scheme, in a fcc crystal matrix, a single layer of hcp atoms represents a twin boundary, two adjacent hcp atom layers manifest an intrinsic stacking fault, and two hcp atom layers with a sandwiched fcc atom layer represent an extrinsic stacking fault.

The visualization tool ATOMEYE (Ref. 28) was used in this work to produce illustrations of defect structures of bicrystals. In ATOMEYE, a parameter called “least-square atomic strain” can be calculated,²⁹ and it was also employed to aid the analysis of the structure transformation processes in the bicrystals. This parameter defines a full transformation matrix \mathbf{J} between the reference configuration $\{\mathbf{x}_i^0\}$ and the present configuration $\{\mathbf{x}_i\}$. Here, \mathbf{x}_i^0 and \mathbf{x}_i are the coordinates of the atom i in the two configurations. In particular, the local transformation matrix \mathbf{J}_i of the atom i gives the best map of $\mathbf{d}_{ji}^0 \rightarrow \mathbf{d}_{ji}$ ($\forall j \in \mathbf{N}_i^0$) based on the least-square fitting method. Here, $\mathbf{d}_{ji}^0 \equiv \mathbf{x}_j^0 - \mathbf{x}_i^0$, $\mathbf{d}_{ji} \equiv \mathbf{x}_j - \mathbf{x}_i$, and \mathbf{N}_i^0 is the set of neighbors of atom i in the reference configuration.

III. RESULTS

A. GB structure and energy

Two optimized structures of the $\Sigma 9 \langle 110 \rangle \{ 221 \}$ symmetric tilt GB have been found at 0 K for all the three metals studied. Figures 2(a) and 2(b) give the two optimized GB structures resulted from the energy minimization procedure and subsequent MD annealing at 300 K and zero stress state for Cu. The structure given in Fig. 2(a) has glide mirror symmetry with the GB plane as the mirror plane while the structure given in Fig. 2(b) has mirror symmetry with the GB plane as its mirror plane. According to the structural unit model,^{1,30} the structure given in Fig. 2(a) is composed of a sequence of the E structural units while the structure given in Fig. 2(b) is composed of the E' structural unit (a distorted E structural unit) and the D structural unit (the structural unit for the coherent twin boundary) one by one. The two optimized

structures of the GB obtained for Al are very similar to those for Cu. However, for Ni, while one of the optimized structures is also composed of the E structural units and it closely resembles the structure given in Fig. 2(a) as well, the other structure [see Fig. 2(c)] shows a minor distortion as compared with the structure given in Fig. 2(b). It can be seen that the distortion breaks the mirror symmetry to some extent. For convenience, GBs with the two kinds of structures will be termed as “E-units” boundaries and “mirror symmetry” boundaries, respectively.

Figure 3 gives the dichromatic pattern of the bicrystal for the $\Sigma 9 \langle 110 \rangle \{ 221 \}$ symmetric tilt GB. By choosing the deep blue balls as the upper crystal and the light yellow balls as the lower crystal, and taking the dashed line I_1 as the inter-

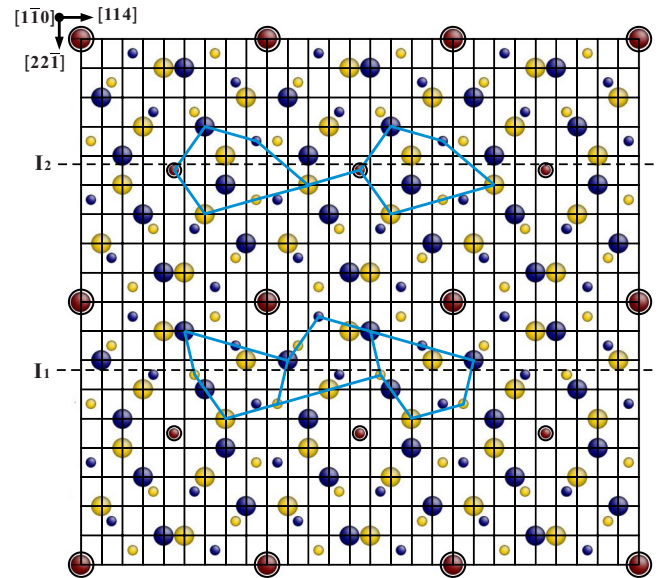


FIG. 3. (Color online) The dichromatic pattern of the bicrystal for GBs with the misorientation relation given by $\Sigma = 9$, $\langle 110 \rangle$ tilt in fcc crystals. The two interpenetrating crystals are represented by the balls with the color deep blue (the upper crystal) and the color light yellow (the lower crystal). The ringed balls are coincidence sites. The fine grid gives the DSC lattice. Balls of two different sizes correspond to the two alternating $(2\bar{2}0)$ lattice planes along the tilt axis $[1\bar{1}0]$.

TABLE II. The GB energy calculated for the two optimized structures of the $\Sigma 9\langle 110\rangle\{221\}$ symmetric tilt GB at 300 K for the three metals.

GB structure	GB energy (mJ m ⁻²)		
	Cu	Al	Ni
E units	825	435	1371
Mirror symmetry	858	468	1432

face plane, the GB structure obtained (the blue solid lines near I_1) then agrees well with the structure given in Fig. 2(a). On the other hand, if we choose the dashed line I_2 as the interface plane and discard the layer of deep blue balls directly above and closest to the interface plane, the GB structure obtained (the blue solid lines near I_2) then corresponds to the structure given in Figs. 2(b) and 2(c) with minor deviations. Thus it can be inferred that the two optimized structures obtained for all the three metals agree well with the CSL description.

It should be mentioned that, both kinds of structures were observed in previous high-resolution electron microscopy studies for Cu (Refs. 31 and 32) and Al (Ref. 33). The experimental results also agree well with the structures given in Figs. 2(a) and 2(b). The GB energy calculated for these optimized structures at 300 K are listed in Table II. It can be seen that the energy of the mirror symmetry boundary at 300 K is slightly larger than that of the E-units boundary for all three metals.

B. Stress-strain behavior of the bicrystals under shear loading at room temperature

The E-units boundaries were selected as the initial structures for the study of the room-temperature shear response of the $\Sigma 9\langle 110\rangle\{221\}$ symmetric tilt GB. Stress-strain curves for shear of the Cu, Al, and Ni bicrystals along the six directions

parallel to the GB plane loaded at 300 K are given in Figs. 4(a)–4(c), respectively. For each straining simulation, the bicrystal was loaded to a total strain of 0.20 along the shear direction. Several features can be perceived from these curves as follows.

(1) The curves for shear along $[1\bar{1}0]$ (red), $[5\bar{4}2]$ (green), $[\bar{1}22]$ (orange), and $[2\bar{1}2]$ (violet) display a regularly serrated profile, which is in agreement with the so-called “stick-slip” behavior of GB sliding.^{34–36} While the “stick” stages correspond to the elastic straining processes, the “slip” events should be related to some kind of structure transformation processes occurring within the bicrystals.

(2) The curves for shear along $[1\ 1\ 4]$ (black) and $[0\bar{1}\bar{2}]$ (blue) are much more irregular. A significant drop of stress levels can be identified for shear of the Al and Ni bicrystals along these two directions. However, this is not the case for shear of the Cu bicrystals along the same directions.

(3) For the shear processes displaying stick-slip behavior as described in (1), most of the curves have a unique peak stress and a certain level of stress relaxation in the slip events. However, for shear of the Cu bicrystal along $[5\bar{4}2]$ [the green curve in Fig. 4(a)], there are mainly two different peak stresses on the stress-strain curve. For shear of the Ni bicrystal along $[2\bar{1}2]$ [the violet curve in Fig. 4(c)], two different levels of stress relaxation can be identified.

(4) It should be mentioned that $[\bar{1}22]$ and $[2\bar{1}2]$ are crystallographically equivalent to each other. Shear of bicrystals along these two directions gives essentially identical stress-strain curves as can be seen from the bottom frames of Figs. 4(a)–4(c) [for the Ni bicrystals, the two curves in the bottom frame of Fig. 4(c) can differ by the level of stress relaxations in some of the slip events, as has been pointed out above].

C. Structure evolution behavior of the bicrystals under shear loading at room temperature

For the study of the structure evolution behavior of the bicrystals, snapshots of atomic configurations of bicrystals

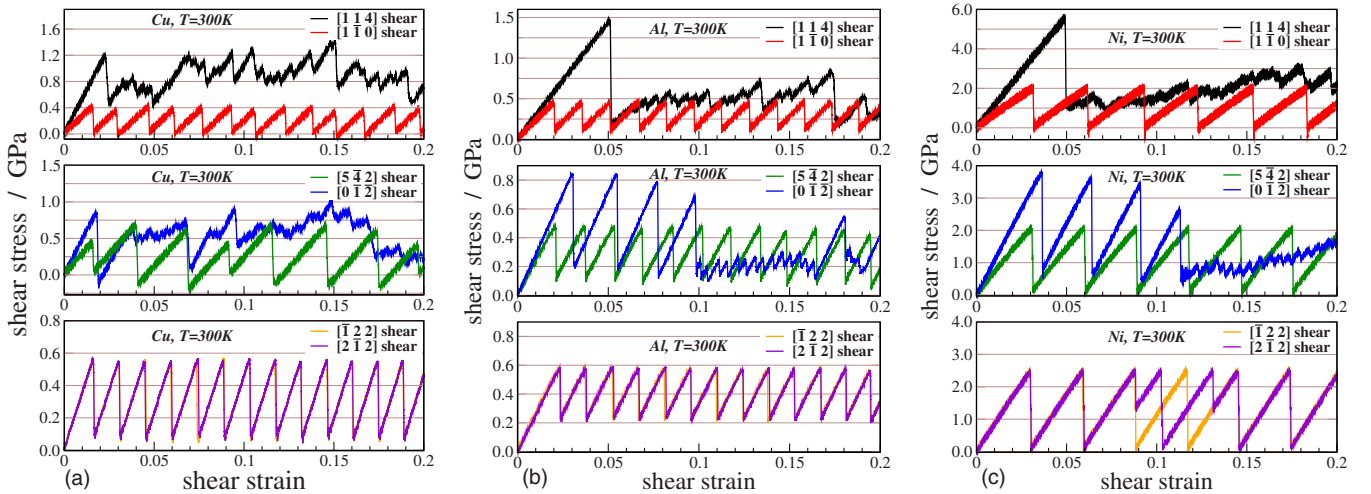


FIG. 4. (Color online) Stress-strain curves for shear of the (a) Cu, (b) Al, and (c) Ni bicrystals along the six directions parallel to the GB plane. Straining simulations were performed at 300 K and with a constant strain rate of 1×10^8 s⁻¹.

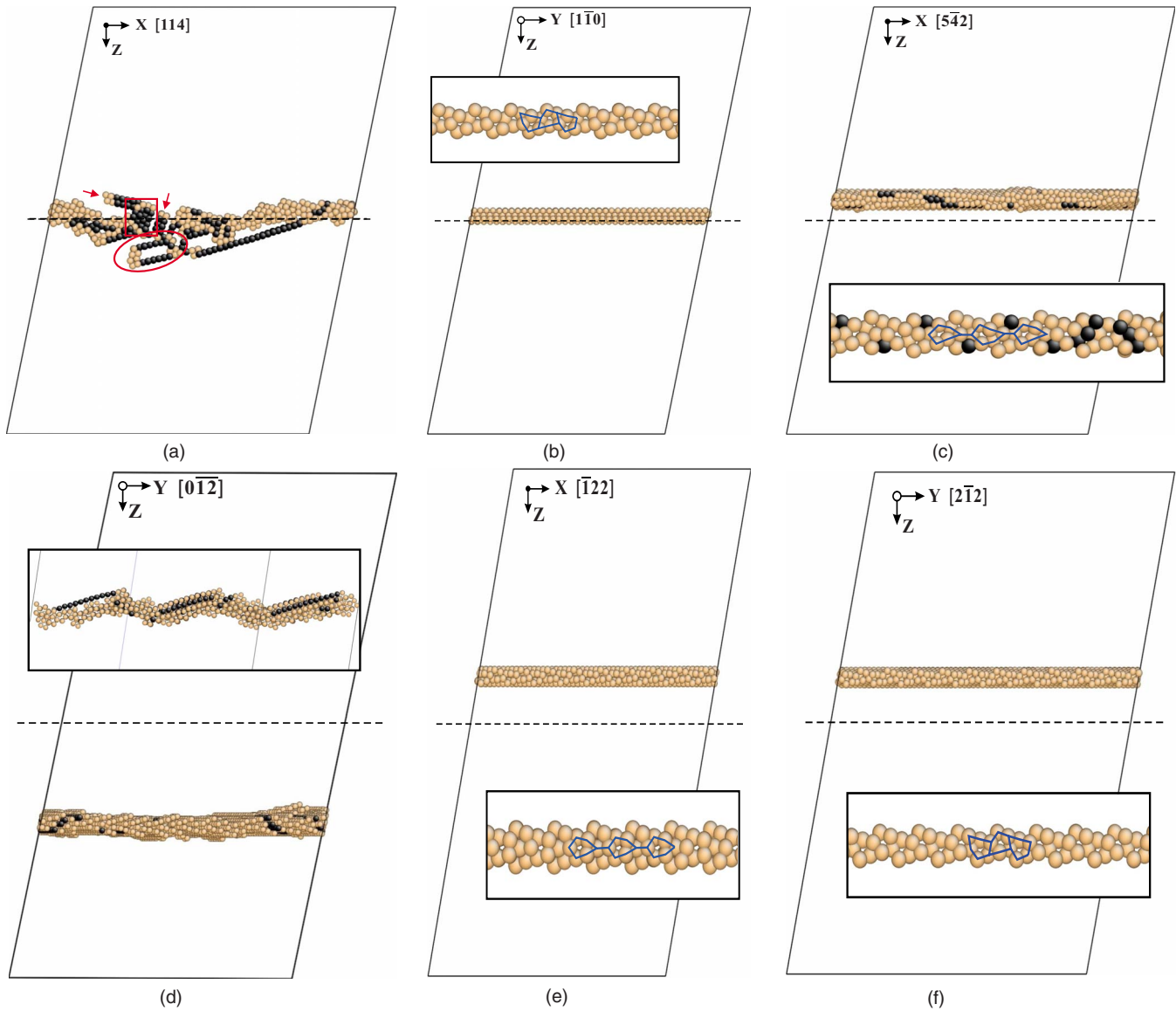


FIG. 5. (Color online) Snapshots of atomic configurations captured at the final steps for shear of the Cu bicrystals along the six directions parallel to the GB plane loaded at 300 K. Only the atoms between the two border slabs which do not have the fcc structural order are displayed. Atoms with hcp structural order are colored as dark while atoms of other structural order are colored as light yellow. Dashed lines mark the initial positions of the GB plane. The insets in (b), (c), and (f) are enlarged view of the $[1\bar{1}0]$ projections of the corresponding snapshots. The insets in (d) and (e) are $[1\bar{1}0]$ projections of the snapshots taken at a shear strain of 0.160 and 0.189, respectively.

were captured every certain number of time steps during the straining simulations. These snapshots were then subjected to a MD quench procedure to remove the thermal noise. Figures 5(a)–5(f) show snapshots captured at the final steps for shear of the Cu bicrystals loaded at 300 K. In these figures, only the atoms between the two border slabs which do not have the fcc structural order are displayed. These atoms constitute the crystal defects within the bicrystals. For the detailed structure evolution processes of all the straining simulations, movies are also provided as supplementary materials associated with this paper.³⁷ For shear of the Cu bicrystals, some features of the structure transformation behavior can be identified as follows.

(1) For the shear along $[1\ 1\ 4]$, Fig. 5(a) shows that lattice dislocations are nucleated and emitted from the GB (see also

movie Cu_S114). These dislocations are leading partials gliding on $\{111\}$ lattice planes as indicated by the arrows in Fig. 5(a). The overlap of the partial dislocations on contiguous $\{111\}$ lattice planes can form twin [the oval in Fig. 5(a)] and hcp structures [the rectangle in Fig. 5(a)]. Meanwhile, detailed analysis indicates that GB sliding and local atomic shuffling activities are accompanied during the straining process (see movie Cu_S114).

(2) For the shear along $[1\bar{1}0]$, Fig. 5(b) shows that the GB stays stationary at its initial position. An examination of the straining process (see movie Cu_S110) reveals that the bicrystal deforms by pure GB sliding processes. In addition, the GB retains its initial structure during the GB sliding processes as can be seen from the inset in Fig. 5(b).

(3) For the shear along $[5\bar{4}2]$, $[0\bar{1}\bar{2}]$, $[\bar{1}22]$, and $[2\bar{1}2]$, Figs. 5(c)–5(f) indicate that the GB has migrated during these straining processes. The migration is accompanied by GB sliding processes and no lattice dislocation activity can be identified (see movies Cu_S542, Cu_S012, Cu_S122, and Cu_S212). Thus it can be perceived that the structure transformation takes the form of GB coupling motions for shear of the Cu bicrystals along these directions.

(4) The GB coupling motions can be different in the direction and distance of GB migration for shear along different directions. For the shear along $[\bar{1}22]$ and $[2\bar{1}2]$, it reveals that the structure of the GB changes between the E-units boundary [the inset in Fig. 5(f)] and the mirror symmetry boundary [the inset in Fig. 5(e)] during the GB coupling motions. However, for the shear along $[5\bar{4}2]$, a transformation of the GB structure between the E-units boundary and a boundary with “quasi-mirror symmetry” [the inset in Fig. 5(c)] results from the GB coupling motion. On the other hand, for the shear along $[0\bar{1}\bar{2}]$, the boundary becomes more disordered during the GB coupling motion (see movie Cu_S012), and sometimes it can be faceted as illustrated by the inset in Fig. 5(d).

For shear of the Al and Ni bicrystals along $[1\bar{1}0]$, $[\bar{1}22]$, and $[2\bar{1}2]$, the structure transformation behavior is very similar to that for shear of the Cu bicrystals along these directions (see movies [Al,Ni]_S110, [Al,Ni]_S122, and [Al,Ni]_S212). However, for shear of the Al and Ni bicrystals along $[1\ 1\ 4]$, $[5\bar{4}2]$, and $[0\bar{1}\bar{2}]$, some different structure transformation behavior can be recognized as compared with those of the Cu bicrystals along the same directions. These differences are summarized as follows.

(1) For shear of the Al bicrystal along $[1\ 1\ 4]$, it shows that GB coupling motion has occurred and no dislocation activity can be identified (see movie Al_S114). Meanwhile, the structure of the GB becomes more disordered. A point defect has been left behind as the GB coupling motion proceeds.

(2) For shear of the Al bicrystal along $[5\bar{4}2]$, GB coupling motion has occurred as well (see movie Al_S542). However, unlike the shear of the Cu bicrystal along this direction, the quasi-mirror symmetry boundary structure cannot be identified. The structure transformation behavior in this case bears a close resemblance to that for shear of the bicrystals along $[\bar{1}22]$ and $[2\bar{1}2]$ [see Figs. 5(e) and 5(f)].

(3) For shear of the Al bicrystal along $[0\bar{1}\bar{2}]$, similar GB coupling motion has occurred as compared with that of the Cu bicrystal along this direction. Disordering of the GB structure can be recognized as well. However, unlike the shear of the Cu bicrystal along this direction, some point defects have been left behind as the GB coupling motion proceeds (see movie Al_S012).

(4) For shear of the Ni bicrystal along $[1\ 1\ 4]$, the nucleation and emission of leading partials can be identified as well (see movie Ni_S114). However, it seems that significant plastic strain is accommodated by GB sliding. A twin structure can also be identified.

(5) For shear of the Ni bicrystal along $[5\bar{4}2]$, no GB coupling motion occurs. The bicrystal deforms by pure GB slid-

ing (see movie Ni_S542). A close examination indicates that the structure of the GB also retains its initial structure during the GB sliding processes.

(6) For shear of the Ni bicrystal along $[0\bar{1}\bar{2}]$, the structure transformation behavior is quite similar to that of the Al bicrystal along the same direction (see movie Ni_S012). The GB becomes more disordered. Meanwhile, there are point defects left behind as the GB coupling motion proceeds.

IV. DISCUSSION

A. Crystallographic analysis of the structure transformations for shear of the $\Sigma 9\langle 110\rangle\{221\}$ symmetric tilt GB

Since the structures of the GBs studied all agree well with the CSL description, the structure transformation mechanisms can be analyzed with the aid of the CSL and the associated DSC lattice for the $\Sigma 9\langle 110\rangle\{221\}$ symmetric tilt GB.^{13,17,38} Additionally, it is also suggested that the GB DSC dislocations that can be responsible for carrying the GB sliding processes should be the ones which have both their Burgers' vectors and step heights as small as possible.³⁹ With this in mind, and together with an examination of the relative displacement of atoms in the GB zone in the slip events, we have been able to identify several elementary structure transformations which can account for the structure evolution behaviors described above. Figures 6(a)–6(f) illustrate six elementary structure transformations (T1–T6) thus identified.

For the T1 transformation as illustrated in Fig. 6(a), the initial GB structure corresponds to the E-units boundary (the blue solid lines in this figure) and the GB plane is aligned with the dashed line I_1 . Suppose the upper crystal (deep blue balls) were displaced relatively to the lower crystal (light yellow balls) according to the red solid arrows near I_1 in this figure, the boundary structure would be transformed to the structural units indicated by the violet dashed lines nearby. The transformed structure gives exactly the mirror symmetry boundary, as can be compared with the blue solid lines near the dashed line I_2 in Fig. 3. Meanwhile, the transformation resulted in migration of the GB plane to the upper crystal by two atom layers ($A \rightarrow \bar{A}$ and $B \rightarrow \bar{B}$).

To account for the feasibility of this transformation, a projection of the lattice part between the two dotted lines X_1 and X_2 in Fig. 6(a) along $[22\bar{1}]$ (the normal of the GB plane) is given in Fig. 7(a). A close examination shows that the displacement vectors of the T_1 transformation (represented by \vec{AA} , \vec{BB} , \vec{CC} , and \vec{DD}) all have a component within the GB plane equal to $\frac{1}{18}[5\bar{4}2]$. On the other hand, as shown in Fig. 6(a), most of the atoms in the upper crystal move up by a layer of $(22\bar{1})$, except that the atoms in the layer second nearest to the GB plane I_1 (represented by the deep blue balls B) move down by a layer of $(22\bar{1})$.

The T2–T6 transformations which are illustrated in the Figs. 6(b)–6(f) can be analyzed in the same way. The displacement vectors of these structure transformations can be mapped onto the lattice part between the two dotted lines X_1 and X_2 in Fig. 6(a) [or Fig. 6(c)], and their $[22\bar{1}]$ projections are also given in Fig. 7(a). A compilation of the initial and

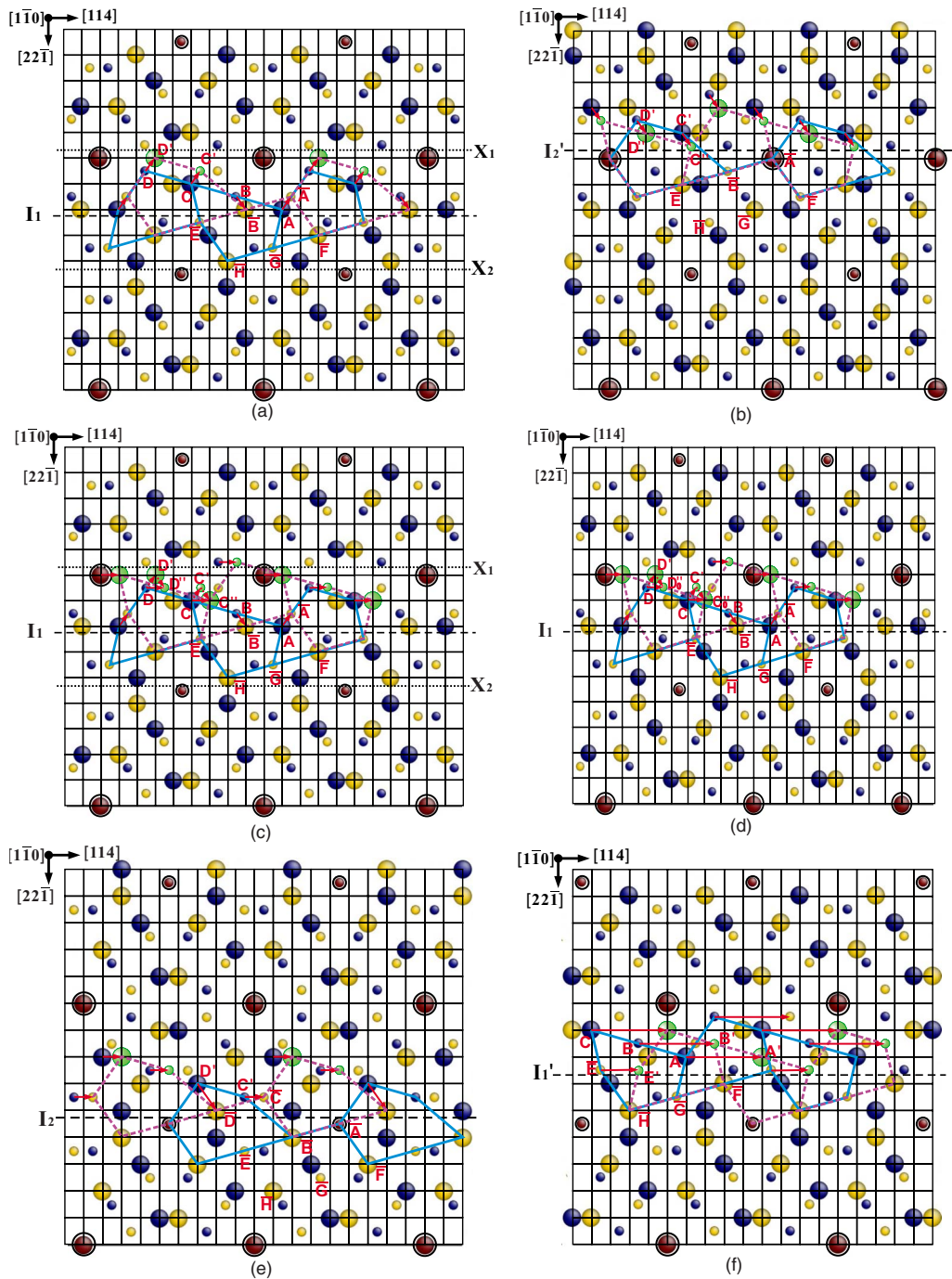


FIG. 6. (Color online) (a)–(f) illustrate the six elementary structure transformations T1–T6 for shear of the $\Sigma 9\langle 110 \rangle \{221\}$ symmetric tilt GB, respectively. The dichromatic pattern the same as that in Fig. 3 is used to give illustration of these structure transformations. Deep blue balls [including A, B, C, D in (a), (c), (d), (f) and C', D' in (b), (e)] represent the lattice sites of the upper crystal and light yellow balls (including $\bar{A}, \bar{B}, \bar{C}, \bar{D}, \bar{E}, \bar{F}, \bar{G}, \bar{H}$) represent the lattice sites of the lower crystal. The ringed balls are coincidence sites. The fine grid gives the DSC lattice. The light green balls are sites resulted from the displacement of the sites of the upper or lower crystals in the structure transformations and are marked by the corresponding letters of their original sites with superscripts (\prime) or ($\prime\prime$). The red arrows are the representative displacement vectors of these structure transformations. Balls marked by the same letters in different frames can be mapped to each other. Balls of two different sizes correspond to the two kinds of alternating $(2\bar{2}0)$ lattice planes along the tilt axis $[1\bar{1}0]$.

transformed structures of GBs, their representative displacement vectors, the migration distances of the GBs, and the characteristic shear directions of these structure transformations are given in Table III. The characteristic shear direction for a particular structure transformation corresponds to the

in-plane component of the overall displacement of the bicrystals in the transformation.

In addition to the T1–T6 transformations, a pure GB sliding transformation (denoted as SI transformation) can also be identified by considering a displacement of the upper crystal

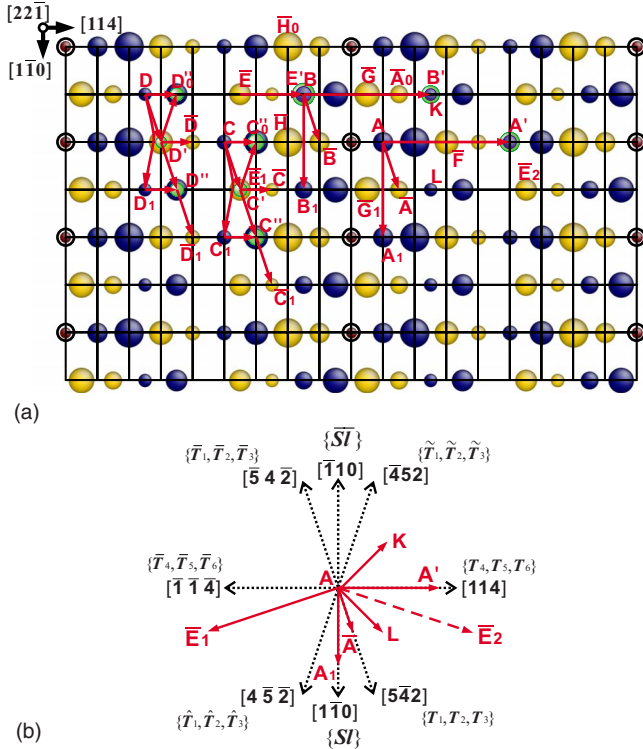


FIG. 7. (Color online) (a) is a projection of the lattice part between the two dotted lines X_1 and X_2 marked in Fig. 6(a) or Fig. 6(c) (with nine lattice planes) along $[22\bar{1}]$. The color scheme is the same as that of Fig. 6. Different sizes of balls in this figure represent different lattice planes along $[22\bar{1}]$ with the smaller balls lying above the bigger ones. Balls marked by the letters the same as those in Fig. 6 are corresponding sites. Balls marked by the same letters but with subscripts “0,” “1,” or “2” are equivalent sites of the ones without subscripts. The deep blue balls K and L are marked to facilitate the specification of shear directions. (b) is a schematic illustration of the characteristic shear directions (the black dotted arrows). The elementary structure transformations corresponding to each characteristic shear direction are given in the braces aside. The six shear directions selected for the study of the shear response of the $\Sigma 9\langle 110\rangle\{221\}$ symmetric tilt GB in this work are indicated by the red arrows $\overline{AA'} = \frac{2}{9}[114]$, $\overline{AA_1} = \frac{1}{2}[1\bar{1}0]$, $\overline{AA} = \frac{1}{18}[5\bar{4}2]$, $\overline{AE_1} = \frac{1}{2}[0\bar{1}2]$, $\overline{AK} = \frac{1}{6}[\bar{1}22]$, and $\overline{AL} = \frac{1}{6}[2\bar{1}2]$ [here, the letters A , A_1 , \bar{A} , A' , K , L , \bar{E}_1 , and \bar{E}_2 represent the corresponding sites marked in (a)]. These directions correspond to the positive directions of the x or y axis of the three orientations of bicrystals (see Fig. 1).

relative to the lower crystal according to the vectors represented by $\overline{AA_1}$ and $\overline{BB_1}$ in Fig. 7(a). These vectors are all equal to $\frac{1}{2}[1\bar{1}0]$, which is the Burgers' vector of a lattice dislocation gliding along the GB plane. Thus both the position and the structure of the GB will not be changed by this transformation.

By considering the symmetry of the $\Sigma 9\langle 110\rangle\{221\}$ symmetric tilt GB [see Fig. 7(a)], it can be concluded that there are three kinds of characteristic shear directions parallel to the GB plane associated with these elementary structure transformations [see the diagram in Fig. 7(b)]: $\langle 5\bar{4}2\rangle$ for the T_1 , T_2 , T_3 transformations and their symmetric counterparts,

$\langle 114\rangle$ for the T_4 , T_5 , T_6 transformations and their opposite ones, and $\langle 1\bar{1}0\rangle$ for the pure GB sliding transformations $\overline{S\bar{L}}$ and \overline{SL} . It should be mentioned that the T_3 transformation is a combination of the T_1 and T_2 transformations, and the T_4 transformation is a combination of the T_1 and \tilde{T}_2 (or \tilde{T}_1 and T_2) transformations, as can be illustrated by the red dashed arrows in Figs. 6(c) and 6(d).

These elementary structure transformations are consistent with GB DSC dislocation mechanisms. The overall displacement vectors and GB migration distances of these elementary structure transformations as presented in Table III can be related to the Burgers' vectors and step heights of the GB DSC dislocations associated with them. On the other hand, the motions of atoms with displacements different than the overall displacement of the bicrystals (see Table III) can be generally regarded as atomic shuffling motions for the passage of these GB DSC dislocations through the GB plane.

For the shear of the Cu bicrystal along $[5\bar{4}2]$, two other structure transformations T_7 and T_8 as illustrated in Fig. 8 and Table III can also be identified. The $[22\bar{1}]$ projections of their representative displacement vectors are given in Fig. 7(a) as well. It is noted that the T_7 transformation is responsible for the production of the boundary structure with the quasi-mirror symmetry as indicated by the inset in Fig. 5(c), and the combination of the T_7 and T_8 transformations also gives the T_3 transformation.

It should be borne in mind that the above analysis is a crystallographic consideration in essence. If the interatomic potentials are taken into consideration, relaxation of the atoms in the GB area would result in the distortion of the GB structure as shown in Fig. 2. In this circumstance, the motions of atoms underlying the elementary structure transformations may differ somewhat from those described above. For example, in Fig. 6(e), the two atom layers of $(22\bar{1})$ in the core of the mirror symmetry boundary as represented by the balls \bar{A} and \bar{B} can be merged into one layer [see the Fig. 2(b)]. Thus the distance for the atoms shuffling along $D' \rightarrow \bar{D}$ across layers of $(22\bar{1})$ can be much reduced in the T_5 transformation.

B. Details of the structure transformation mechanisms for shear of the bicrystals along the six directions

To see how the elementary structure transformations described above are related to the structure evolution behavior of bicrystals during the straining processes, the displacement of bicrystals in the direction perpendicular to the shear direction and parallel to the GB plane (i.e., the side displacement of bicrystals) can be used to aid the analysis. If the characteristic shear direction of an elementary structure transformation occurred within the bicrystal is not aligned with the shear direction, a jump of the side displacement of the bicrystal would result. For a given shear direction, the distance and direction of jumps can be different for different elementary structure transformations. By calculating the side displacement of the bicrystal for shear along a particular direction, elementary structure transformations with different side displacements induced in the bicrystal can then be distin-

TABLE III. A description of the elementary structure transformations T_1 – T_8 and Sl . “E.U.,” “M.S.,” and “Q.M.S.” stand for the E-units, mirror symmetry, and quasi-mirror symmetry boundary structures, respectively. In the column of the representative displacement vectors within the [] correspond to displacements of atoms with shuffling motions involved while others correspond to the overall displacement of the bicrystals. These vectors are illustrated in both Figs. 6 and 7(a). The unit for the GB migration distance is the interlayer distance of $(22\bar{1})$ layers, which is equal to $|\frac{1}{18}[22\bar{1}]|$. A negative migration distance signifies that the GB migrates down in the bicrystal. The characteristic shear direction corresponds to the in-plane component of the overall displacement of the bicrystals in the transformation.

Structure transformation	Initial GB structure	Transformed GB structure	Representative displacement vectors	GB migration distance	Characteristic shear direction
T_1	E.U.	M.S.	\overline{AA} , $[\overline{BB}]$, $\overline{CC'}$, $\overline{DD'}$	2	$[5\bar{4}2]$
T_2	M.S.	E.U.	$\overline{C'C''}$, $\overline{D'D''}$	0	$[5\bar{4}2]$
T_3	E.U.	E.U.	$[\overline{AA}, \overline{BB}]$, $\overline{CC''}$, $\overline{DD''}$	2	$[5\bar{4}2]$
T_4	E.U.	E.U.	$[\overline{AA}, \overline{BB}]$, $\overline{CC'_0}$, $\overline{DD'_0}$	2	$[114]$
T_5	M.S.	M.S.	$\overline{C'C}$, $[\overline{D'D}]$	2	$[114]$
T_6	E.U.	E.U.	$[\overline{EE'}]$, $\overline{AA'}$, $\overline{BB'}$	–1	$[114]$
T_7	E.U.	Q.M.S.	$[\overline{AA}, \overline{BB}]$, $\overline{CC_1}$, $\overline{DD_1}$	2	$[1\bar{1}0]$
T_8	Q.M.S.	E.U.	$\overline{C_1C''}$, $\overline{D_1D''}$	0	$[114]$
Sl	E.U./M.S.	E.U./M.S.	$\overline{AA_1}$, $\overline{BB_1}$	0	$[1\bar{1}0]$

guished. The curves of the side displacement of bicrystals for the straining processes simulated at 300 K are given in Fig. 9 for all the three metals. The side displacement of the bicrystals was calculated by the relative in-plane displacement of center of mass of the two border slabs in the direction perpendicular to the shear direction.

It is expected that for shear of the bicrystals along a given direction, the elementary structure transformations activated should be the one(s) with the characteristic shear direction(s) as close to the shear direction as possible. With the guidance of the diagram in Fig. 7(b), and together with a combined examination of the side displacement curves and the structure evolution behavior of the bicrystals, detailed structure transformation mechanisms for shear of the bicrystals along the six directions can be gained.

Take the shear along $[2\bar{1}2]$ as an example. The bicrystals deform by GB coupling motions for all the three metals as illustrated in Fig. 5(f) and the movies [Cu,Al,Ni]_S212. The violet curves in Fig. 9 suggest that the GB coupling motions are realized by the $T_3(=T_1+T_2)$ transformation. This can be understood by an examination of the diagram in Fig. 7(b). The shear direction is aligned with \overline{AL} in Fig. 7(b). The characteristic shear directions of the T_1 , T_2 , and T_3 transformations all correspond to $[5\bar{4}2]$. This direction has an obtuse angle with the positive direction of the x axis of the simulation cell $[\overline{AK}]$ in Fig. 7(b). A negative jump of the side displacement of bicrystal can then result in the occurrence of these structure transformations as illustrated by the violet curves in Fig. 9.

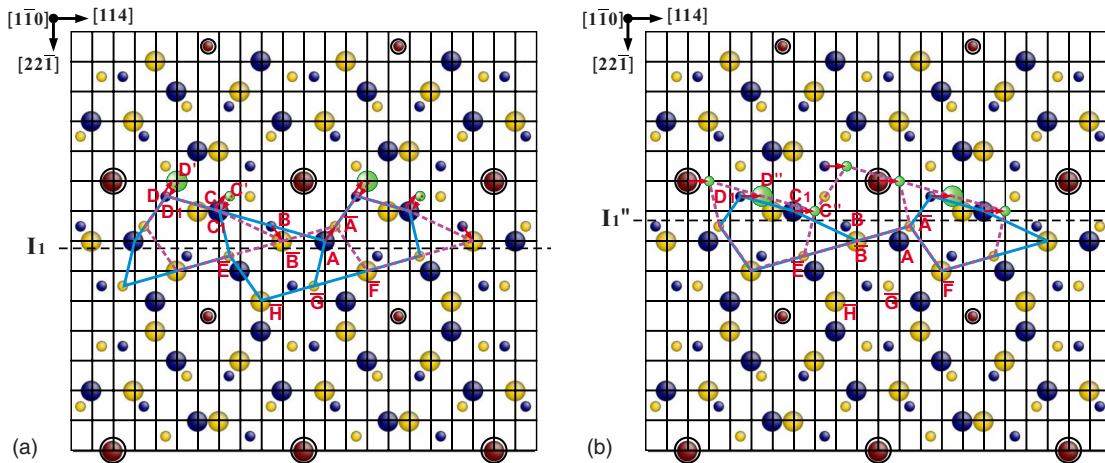


FIG. 8. (Color online) Structure transformations (a) T_7 and (b) T_8 for shear of the $\Sigma 9\langle 110 \rangle \{221\}$ symmetric tilt GB. The dichromatic pattern used here is the same as those in Fig. 6.

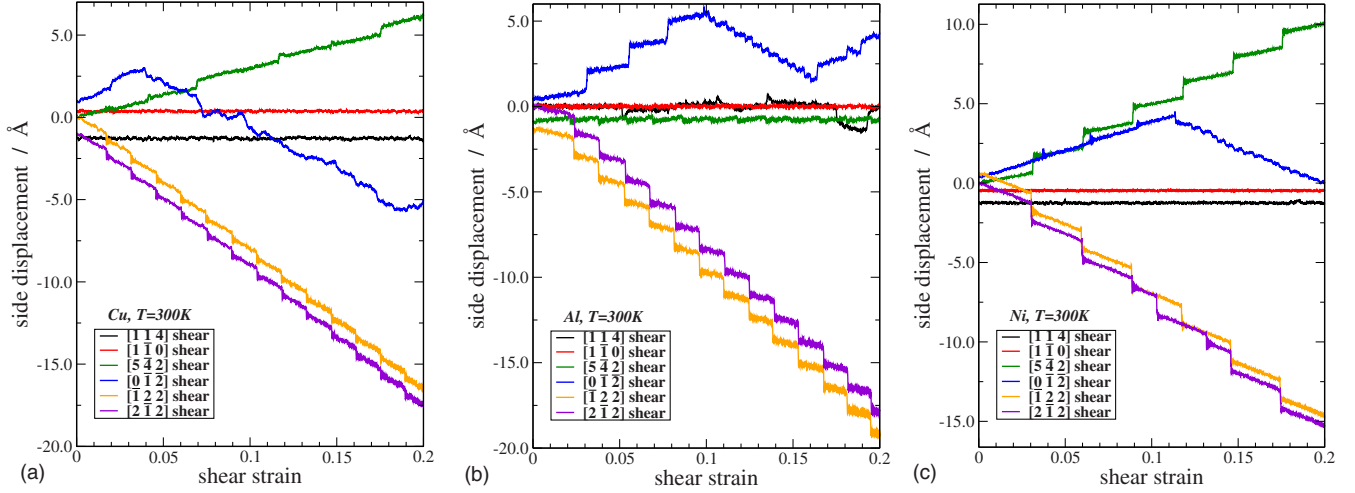


FIG. 9. (Color online) The curves of the side displacement of bicrystals for the straining processes as described above. These curves can be related to the stress-strain curves in Fig. 4 correspondingly. Some of the curves have been slightly shifted along the vertical axes for clarity.

For shear along other directions, similar analysis can be performed, and the results are summarized in Table IV. For shear of the bicrystals along $[\bar{1}22]$, it gives essentially identical mechanical behavior as with that for shear along $[2\bar{1}2]$. Thus only the results for the latter ones are given.

In Fig. 7, it can be seen that shear of the upper crystal along $[0\bar{1}2](A\bar{E}_1)$ is crystallographically equivalent to shear of the lower crystal along $A\bar{E}_2$ [should invert the upper and lower crystals in Fig. 7(a) in this case, i.e., deep blue balls for the lower crystal and light yellow balls for the upper crystal]. Thus the shear direction $A\bar{E}_2$ can be considered instead of $A\bar{E}_1$ for the analysis.

For shear of the bicrystals along $[5\bar{4}2]$, different metals display a different structure evolution behavior. By an examination of the Figs. 6(c) and 7(a), it is inferred that the differences in the structure transformation behavior can be attributed to the energy barrier formed along the $C \rightarrow C' \rightarrow C''$ path for the displacement of atoms in the layer C (and together with the atoms above it) through the layer of atoms as represented by the light yellow balls \bar{E}_1 or \bar{E} . For the Cu and Ni bicrystals, this energy barrier should be comparatively high. The T_7 , T_8 , and SI transformations are thus adopted instead of the T_3 transformation.

For shear of the Cu and Ni bicrystals along $[1\ 1\ 4]$, lattice dislocations nucleation and emission from the GBs can be identified (see movies Cu_S114 and Ni_S114). GB sliding and local atomic shuffling activities are also accompanied during the straining processes. The GB sliding should be realized by a combination of the T_4 and T_6 transformations. Both the upward GB migration (T_4) and the downward GB migration (T_6) coexist and can thus cancel each other. It is quite likely that the competition between these elementary structure transformations under a high external stress results in uncoordinated atomic shuffling activities localized in the GB area, which in turn causes stress concentration nearby. The nucleation and emission of lattice dislocations can then be favored.

However, for shear of the Al bicrystal along $[1\ 1\ 4]$, the bicrystal deforms by GB coupling motions. The reason that lattice dislocation nucleation and emission does not occur in this case can be related to the morphology of the γ surface of the GB and the general stacking fault energy surface for Al with the interatomic potential employed.⁴⁰

For shear of the bicrystals along $[1\ 1\ 4]$ and $[0\bar{1}2]$, the GB structures become quite disordered, and sometimes point defects can be generated [see Figs. 5(a) and 5(d), and the movies [Cu,Al,Ni]_S114 and [Cu,Al,Ni]_S012). It seems that the disordering of the GB structures and the generation of the

TABLE IV. Structure transformation mechanisms and the corresponding pair parameter (λ, κ) calculated for shear of the bicrystals of all the three metals as described above. The structure transformation mechanisms are given by the elementary structure transformations involved in the straining processes. The elementary structure transformations T_1 – T_8 and SI are described in Table III. $\hat{T}_1, \hat{T}_2, \hat{T}_3, \hat{T}_4, \hat{T}_5$ are the symmetry counterpart of T_1, T_2, T_3, T_4, T_5 [see Fig. 7(b)]. “D” stands for lattice dislocation nucleation and emission from the GB. For the shear processes with lattice dislocations emitted from GB, GB migration is not a well-defined feature, thus the λ value is not given.

Shear direction	$[1\ 1\ 4]$	$[1\bar{1}0]$	$[5\bar{4}2]$	$[0\bar{1}2]$	$[2\bar{1}2]$
Cu	$T_4/T_6/D (\times, 0)$	$SI (0,0)$	$T_7/T_8/SI (0.184, 0.180)$	$\hat{T}_3/\hat{T}_4 (-1.065, -0.177)$	$T_3 (0.485, -0.507)$
Al	$T_4/T_6/T_1/\hat{T}_2 (0.719, 0)$	$SI (0,0)$	$T_3 (0.434, 0)$	$\hat{T}_1/\hat{T}_2/\hat{T}_5 (-1.220, 0.105)$	$T_3 (0.486, -0.492)$
Ni	$T_4/T_6/D (\times, 0)$	$SI (0,0)$	$SI (0, 0.344)$	$\hat{T}_1/\hat{T}_2/\hat{T}_5 (-1.139, -0.012)$	$T_3 (0.488, -0.527)$

point defects can also be attributed to the uncoordinated shuffling of atoms in the GB area as a result of the competition between the various elementary structure transformations involved.

C. Association of the structure transformation mechanisms to the stress-strain curves

The stress-strain response of the bicrystals as illustrated in Fig. 4 can also be associated with the structure transformation mechanisms presented in Table IV. For the shear processes with a single type of elementary structure transformation involved, a regular stick-slip behavior of the stress-strain response generally result (e.g., shear of the bicrystals along $[1\bar{1}0]$ and $[2\bar{1}2]$). The peak stresses in the stick-slip behavior can be related to the critical shear stress for the initiation of the elementary structure transformation involved, with also a consideration of the angle between the shear direction and the characteristic shear direction of this transformation (a Schmid-type effect).¹⁷ For the shear processes with various types of elementary structure transformations involved, a much more irregular stress-strain response of the bicrystals can be gained as illustrated by the black and blue curves in Fig. 4.

For shear of the Al and Ni bicrystals along $[0\bar{1}2]$, a significant drop of the stress levels can be recognized on the blue curves in Figs. 4(b) and 4(c). It is noted that the occurrence of the drop of the stress levels is associated with the change in direction of the side displacement of bicrystals as illustrated by the blue curves in Figs. 9(b) and 9(c). This implies that a change in the structure transformation mechanism from the T_1 and T_2 transformations to the T_3 transformations is responsible for the drop of the stress levels. For further verification of this point, straining simulations for shear of the bicrystals along $[1\ 1\ 4]$ with the mirror symmetry boundaries as the initial GB structure were performed for the three metals. A loading temperature of 300 K and the constant strain rate of $1 \times 10^8\ \text{s}^{-1}$ were used. The stress-strain curves and the side displacement curves were obtained. Movies of the detailed structure evolution processes for these three shear processes are provided as supplementary material associated with this article.³⁷

For shear of the Al and Ni bicrystals along $[1\ 1\ 4]$ with the mirror symmetry boundaries as the initial GB structure, the stick-slip behavior can also be identified on the stress-strain curves. The levels of the peak stresses on these two stress-strain curves are found to be comparable with the lower levels of stresses on the blue curves in Figs. 4(b) and 4(c) correspondingly. With a combined examination of the structure evolution behavior (see movies Al_Symt_S114 and Ni_Symt_S114) and the side displacement of bicrystals, it shows that the bicrystals deform by GB coupling motions which are realized by a series of the T_5 transformations for these two straining processes. It can thus be concluded that the drop of the stress levels for shear of the Al and Ni bicrystals along $[0\bar{1}2]$, as illustrated by the blue curves in Figs. 4(b) and 4(c), should be attributed to the transition of the structure transformation mechanism from the T_1 and T_2 transformations to the T_5 transformation.

A drop of the stress levels can also be recognized on the black curves in Figs. 4(b) and 4(c) for shear of the Al and Ni bicrystals along $[1\ 1\ 4]$. However, since the GBs become significantly disordered during these two shear processes, we could not identify for sure whether or not a transition of structure transform mechanisms are in effect in a similar way.

On the other hand, for shear of the Cu bicrystal along $[1\ 1\ 4]$ with the mirror symmetry boundary as the initial GB structure, the structure of the GB first transforms to the E-units boundary at a fairly low stress level (around 120 MPa). The succeeding structure evolution behavior and the stress-strain response then resemble that for shear of the Cu bicrystal along this direction but with the E-units boundary as the initial GB structure. This illustrates that the mirror symmetry boundary structure is not stable under shear stress for the Cu bicrystal. Thus the T_5 transformation cannot be involved for shear of the Cu bicrystals. The much more irregular stress-strain curves for shear of the Cu bicrystals along $[1\ 1\ 4]$ and $[0\bar{1}2]$ [the black and blue curves in Fig. 4(a)] should have something to do with the particular morphology of the γ surface of the GB for Cu with the interatomic potential employed.

D. GB disconnection mechanisms for the structure transformations

Although the slip events occur almost instantly once the peak shear stresses have been reached, the underlying structure transformations may not take place uniformly across the GB plane. It is suggested that the nucleation and expansion of GB disconnections (interface line defects with both dislocation and step character^{39,41,42}) can be responsible for the GB coupling motions.^{17,34,43} A close examination of the slip processes reveals that this GB disconnection mechanism can also be identified.

Figure 10 shows a snapshot captured in the first slip event for shear of the Ni bicrystal along $[\bar{1}22]$. A GB disconnection which is expanding through the GB plane can be seen. The step feature of this GB disconnection is illustrated in Figs. 10(a) and 10(b). It can be seen that the step has a height of two $(22\bar{1})$ layers, which is consistent with the above analysis that the GB coupling motions in this case are realized by the T_3 transformation (the combination of the T_1 and T_2 transformations). The dislocation feature is demonstrated in Fig. 10(c). The entire transformation process which accounts for this slip event can be illustrated by the movies Ni_gbd122_a and Ni_gbd122_b in the supplementary materials associated with this paper.³⁷ It is found that there are two such GB disconnections nucleated and expanded through the GB plane one after the other in this slip event. The smaller level of stress relaxation on the violet curve in Fig. 4(c) should correspond to a single GB disconnection activated during the slip processes.

GB disconnections can also be identified in other slip processes for shear of the Al and Ni bicrystals. However, it is found that several GB disconnections can nucleate simultaneously at different areas of the GB plane for shear of the Al bicrystals. On the other hand, for shear of the Cu bicrystals,

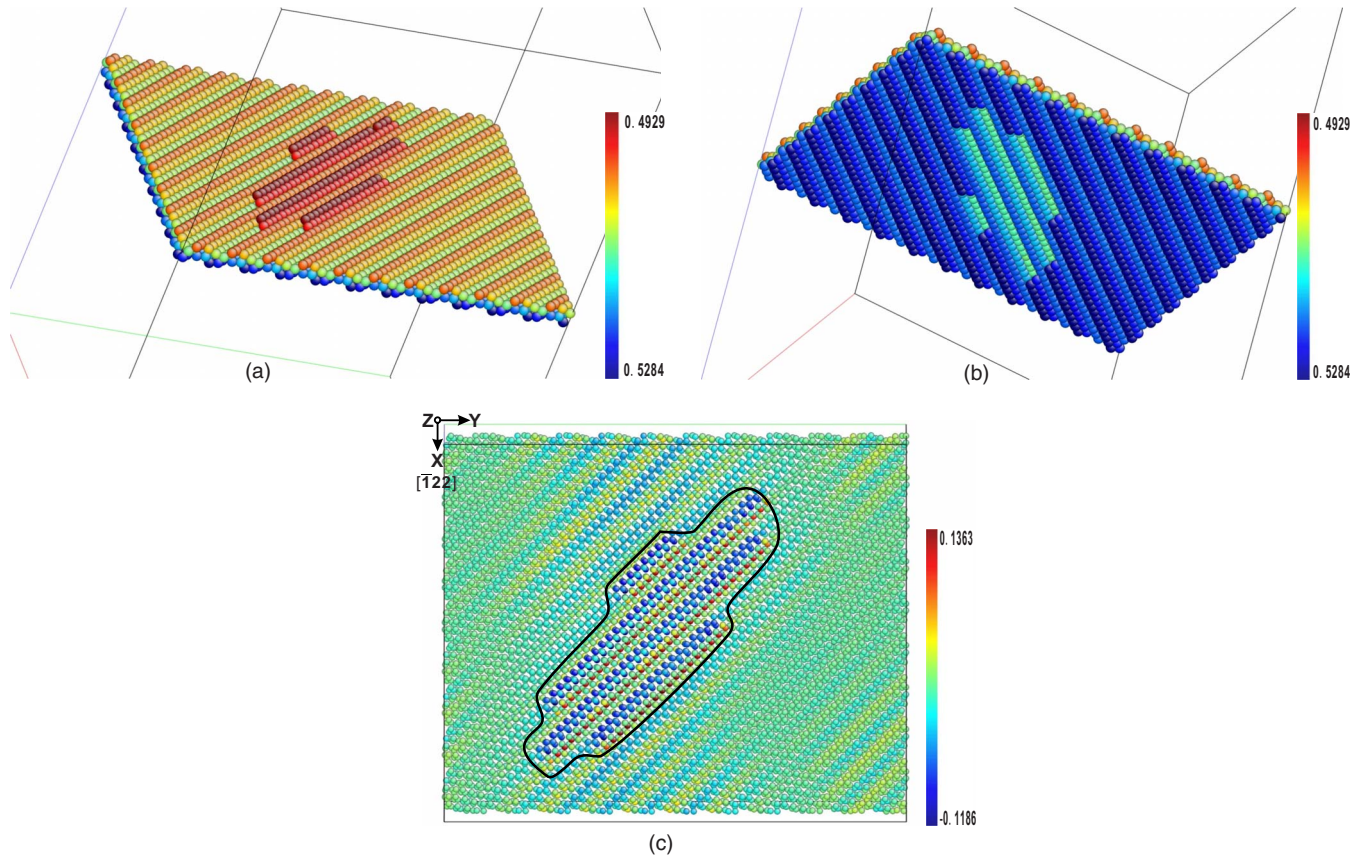


FIG. 10. (Color online) A GB disconnection nucleated homogeneously in the first slip event for shear of the Ni bicrystal along $[\bar{1}22]$. (a) and (b) are two views of the GB from the upper and lower sides of the bicrystal, respectively. Atoms displayed are those between the two border slabs which do not have fcc structural order according to the CNA description. The color scales are given as the reduced coordinates of the atoms along the z axis (normal of the GB plane). (c) is a projection of the GB along the normal of the GB plane. All the atoms in the relevant layers which appear in (a) and (b) are displayed. The color scale in this panel is given as the J_{yz} component of the least-square atomic strain of each atom. A bicrystal configuration a few tens steps before the occurrence of the transformation is selected as the reference configuration for the calculation of the least-square atomic strain. The black solid line is given to guide the eyes.

a simultaneously initiation of the structure transformation distributed on the GB plane makes the features of GB disconnection less salient.

E. GB coupling motion analysis

For the description of the GB coupling motions, the coupling factor β , which is defined as the ratio between the sliding distance (S) and migration distance (M) of the GB (i.e., $\beta = S/M$), is usually proposed.^{1,4,43} However, it has been demonstrated in our simulations that there can be side displacement (T) of bicrystals for shear of them along a particular direction if GB coupling motions are involved in the structure transformations [see Fig. 9]. Thus we suggest that a pair parameter (λ, κ) is used to describe the GB coupling motions instead. Here, $\lambda = M/S$ and $\kappa = T/S$. Unlike the coupling factor β , the denominator of λ and κ is specified as the sliding distance S instead of the migration distance M or the side displacement T to avoid the infinity value of the pair parameter for the case where the migration distance or side displacement is zero.

In Table IV, the pair parameters (λ, κ) calculated for each straining process performed in this work are also given. For

each elementary structure transformation and with a given shear direction, a characteristic pair parameter can also be calculated according to the CSL-DSC theory (see Figs. 6 and 7), and the results are given in Table V. If the structure transformation mechanism for a specific shear process is a mixture of various elementary structure transformations, then the ultimate pair parameter should be a weighted summation of the characteristic pair parameters of the elementary structure transformations involved. A comparative examination of the Tables IV and V indicates that the pair parameters given by our simulations are in good agreement with that predicted by the CSL-DSC theory. This in turn lends further credence to the structure transformation mechanisms proposed for these straining processes as given in Table IV.

Although the $\Sigma 9\langle 110 \rangle \{221\}$ symmetric tilt GB is a very specific boundary among all the high-angle GBs, it is reasonable to speculate that there is a family of “special” GBs, special in the sense that GB coupling motions realized by the GB DSC dislocations or GB disconnections can occur on them.¹⁷ However, since there is no well-established criteria to ascertain whether a GB can be classified as special or not, it seems that extended effort should be made to probe for other special GBs. The GB coupling motions may contribute

TABLE V. The characteristic pair parameters (λ, κ) for the elementary structure transformations with the given shear directions as mentioned in Table IV. Note that $T_3 = T_1 + T_2 = T_7 + T_8$ and $T_4 = T_1 + \tilde{T}_2$. For the shear along $[0\bar{1}\bar{2}]$, the elementary structure transformations in the parentheses are considered or else otherwise.

Shear direction	$[1\ 1\ 4]$	$[\bar{1}\bar{1}0]$	$[5\bar{4}2]$	$[0\bar{1}\bar{2}]$	$[2\bar{1}2]$
$T_1(\hat{T}_1)$	(2.828,3)	(0.943,0.333)	(0.894,0)	(-1.491, 1.333)	(1.0, -0.5)
$T_2(\hat{T}_2)$	(0,3)	(0,0.333)	(0,0)	(0,1.333)	(0, -0.5)
\tilde{T}_2	(0, -3)				
$T_3(\hat{T}_3)$	(1.414,3)	(0.471,0.333)	(0.447,0)	(-0.745, 1.333)	(0.5, -0.5)
$T_4(\tilde{T}_4)$	(1.414,0)		(4.472, -3)	(-1.491, -0.333)	(2.0, 1.0)
$T_5(\tilde{T}_5)$	(1.414,0)		(4.472, -3)	(-1.491, -0.333)	(2.0, 1.0)
$T_6(\tilde{T}_6)$	(-0.177, 0)			(0.186, -0.333)	(-0.25, 1.0)
Sl		(0,0)	(0,0.333)		

to the recently reported grain coarsening phenomena observed during plastic deformation of nanocrystalline or ultrafine-grained metals loaded at elevated,⁴⁴ ambient,⁴⁵⁻⁵⁰ or even cryogenic temperatures.^{45,46}

V. SUMMARY

We have performed atomistic simulation studies of the room-temperature shear response of the $\Sigma 9\langle 110 \rangle\{221\}$ symmetric tilt GB in three fcc metals Cu, Al, and Ni. EAM-type interatomic potentials together with a bicrystal model were employed to perform the investigation. Six shear directions parallel to the GB plane have been studied: $[1\ 1\ 4]$, $[\bar{1}\bar{1}0]$, $[5\bar{4}2]$, $[0\bar{1}\bar{2}]$, $[\bar{1}\bar{2}2]$, and $[2\bar{1}2]$. The stress-strain response and the structure evolution behavior of the bicrystals have been analyzed in great detail. The main results are summarized as follows.

(i) There are two optimized structures of this GB for all three metals at zero temperature: the E-units boundary and the mirror symmetry boundary. The E-units boundary structure is found to be the stable structure at room temperature. Both kinds of structures can be well described by the CSL theory.

(ii) For shear of the bicrystals at room temperature, various kinds of structure evolution behavior have been found for this GB depending on the shear direction: (1) pure GB sliding; (2) GB atomic shuffling accompanied by lattice dislocation emission from the GB; and (3) GB coupling motion. The GB coupling motions can differ in the direction and distance of GB migration depending on the shear direction.

(iii) For the shear along $[\bar{1}\bar{1}0]$, $[\bar{1}\bar{2}2]$, and $[2\bar{1}2]$, the structure transformation behavior is very similar for all three metals. For the shear along $[1\ 1\ 4]$, $[5\bar{4}2]$, and $[0\bar{1}\bar{2}]$, some

differences on the structure transformation behavior can be recognized for the different metals.

(iv) Several elementary structure transformations which are inherent to this particular GB have been identified according to the CSL-DSC theory. Three kinds of characteristic shear directions can be recognized with these elementary structure transformations (all parallel to the GB plane): $\langle 5\bar{4}2 \rangle$, $\langle 114 \rangle$, and $\langle 1\bar{1}0 \rangle$. The structure evolution behavior for shear of the bicrystals can be well interpreted by considering these elementary structure transformations as the underlying structure transformation mechanisms. These elementary structure transformations are also consistent with the GB DSC dislocation or GB disconnection mechanisms.

(v) Shear of the bicrystals with a single type of elementary structure transformation activated generally gives a regular stick-slip behavior for the stress-strain response. With more than one type of elementary structure transformation involved, the competition between the transformations can result in a disordering of the GBs, and much more irregular stress-strain response of the bicrystals can be gained. For shear of the Al and Ni bicrystals along $[0\bar{1}\bar{2}]$, a transition of the structure transformation mechanism during the shear processes can lead to a significant drop of stress levels.

(vi) A pair parameter (λ, κ) is proposed to describe the GB coupling motions. For all the GB coupling motions, the pair parameters calculated are in agreement with that predicted by the CSL-DSC theory.

ACKNOWLEDGMENTS

This work is supported by the National Basic Research Program of China (Grant No. 2006CB605103). We would like to acknowledge W. Alan Oates for his kind help on English.

*Corresponding author. FAX: +86 24 23891320; liangwan5@gmail.com

- ¹A. P. Sutton and R. W. Balluffi, *Interfaces in Crystalline Materials* (Clarendon Press, Oxford, 1995).
- ²H. J. Frost and M. F. Ashby, *Deformation-Mechanism Maps: The Plasticity and Creep of Metals and Ceramics* (Pergamon Press, London, 1982).
- ³M. A. Meyers, A. Mishra, and D. J. Benson, *Prog. Mater. Sci.* **51**, 427 (2006).
- ⁴M. F. Ashby, *Surf. Sci.* **31**, 498 (1972).
- ⁵R. Monzen and Y. Sumi, *Philos. Mag. A* **70**, 805 (1994).
- ⁶R. Monzen, Y. Sumi, K. Kitagawa, and T. Mori, *Acta Metall. Mater.* **38**, 2553 (1990).
- ⁷R. Monzen, M. Futakuchi, and T. Suzuki, *Scr. Metall. Mater.* **32**, 1277 (1995).
- ⁸H. Miura, T. Sakai, T. Otsuka, R. Monzen, and S. Onaka, *Acta Mater.* **48**, 1959 (2000).
- ⁹Y. Qi and P. E. Krajewski, *Acta Mater.* **55**, 1555 (2007).
- ¹⁰Y. Mishin, M. Asta, and J. Li, *Acta Mater.* **58**, 1117 (2010).
- ¹¹R. C. Pond, D. A. Smith, and P. W. Southerden, *Philos. Mag. A* **37**, 27 (1978).
- ¹²T. Mori and K. Tangri, *Metall. Trans. A* **10**, 733 (1979).
- ¹³A. H. King, *Acta Metall.* **30**, 419 (1982).
- ¹⁴R. J. Kurtz and R. G. Hoagland, *Scr. Mater.* **39**, 653 (1998).
- ¹⁵R. J. Kurtz, R. G. Hoagland, and J. P. Hirth, *Philos. Mag. A* **79**, 665 (1999).
- ¹⁶B. Hyde, D. Farkas, and M. J. Caturla, *Philos. Mag.* **85**, 3795 (2005).
- ¹⁷L. Wan and S. Wang, *Modell. Simul. Mater. Sci. Eng.* **17**, 045008 (2009).
- ¹⁸H. Fukutomi and T. Kamijo, *Scr. Metall.* **19**, 195 (1985).
- ¹⁹A. D. Sheikh-Ali, *Acta Mater.* **45**, 3109 (1997).
- ²⁰W. Bollman, *Crystal Defects and Crystalline Interfaces* (Springer, Berlin, 1970).
- ²¹H. Grimmer, W. Bollman, and D. H. Warrington, *Acta Crystallogr., Sect. A: Cryst. Phys., Diffr., Theor. Gen. Crystallogr.* **30**, 197 (1974).
- ²²S. J. Plimpton, *J. Comput. Phys.* **117**, 1 (1995).
- ²³S. Melchionna, G. Ciccotti, and B. L. Holian, *Mol. Phys.* **78**, 533 (1993).
- ²⁴M. P. Allen and D. J. Tildesley, *Computer Simulation of Liquids* (Clarendon Press, Oxford, 1987).
- ²⁵Y. Mishin, M. J. Mehl, D. A. Papaconstantopoulos, A. F. Voter, and J. D. Kress, *Phys. Rev. B* **63**, 224106 (2001).
- ²⁶Y. Mishin, D. Farkas, M. J. Mehl, and D. A. Papaconstantopoulos, *Phys. Rev. B* **59**, 3393 (1999).
- ²⁷D. Faken and H. Jonsson, *Comput. Mater. Sci.* **2**, 279 (1994).
- ²⁸J. Li, *Modell. Simul. Mater. Sci. Eng.* **11**, 173 (2003).
- ²⁹F. Shimizu, S. Ogata, and J. Li, *Mater. Trans.* **48**, 2923 (2007).
- ³⁰J. D. Rittner and D. N. Seidman, *Phys. Rev. B* **54**, 6999 (1996).
- ³¹J. R. Hu, S. C. Chang, F. R. Chen, and J. J. Kai, *Mater. Chem. Phys.* **74**, 313 (2002).
- ³²O. H. Duparc, J.-P. Couzinie, J. Thibault-Penisson, S. Lartigue-Korinek, B. Decamps, and L. Priester, *Acta Mater.* **55**, 1791 (2007).
- ³³M. J. Mills, *Mater. Sci. Eng., A* **166**, 35 (1993).
- ³⁴Y. Mishin, A. Suzuki, B. P. Uberuaga, and A. F. Voter, *Phys. Rev. B* **75**, 224101 (2007).
- ³⁵V. A. Ivanov and Y. Mishin, *Phys. Rev. B* **78**, 064106 (2008).
- ³⁶Q. Hu, L. Li, and N. M. Ghoniem, *Acta Mater.* **57**, 4866 (2009).
- ³⁷See supplementary material at <http://link.aps.org/supplemental/10.1103/PhysRevB.82.214112> for movies which give illustrations of the structure evolution processes mentioned in Sec. III C, Sec. IV C, and the GB disconnection activities mentioned in Sec. IV D.
- ³⁸R. G. Hoagland and R. J. Kurtz, *Philos. Mag. A* **82**, 1073 (2002).
- ³⁹R. C. Pond and S. Celotto, *Int. Mater. Rev.* **48**, 225 (2003).
- ⁴⁰V. Vitek, *Philos. Mag.* **18**, 773 (1968).
- ⁴¹J. P. Hirth, *J. Phys. Chem. Solids* **55**, 985 (1994).
- ⁴²J. P. Hirth and R. C. Pond, *Acta Mater.* **44**, 4749 (1996).
- ⁴³J. W. Cahn, Y. Mishin, and A. Suzuki, *Acta Mater.* **54**, 4953 (2006).
- ⁴⁴F. Momprou, D. Caillard, and M. Legros, *Acta Mater.* **57**, 2198 (2009).
- ⁴⁵K. Zhang, J. R. Weertman, and J. A. Eastman, *Appl. Phys. Lett.* **85**, 5197 (2004).
- ⁴⁶K. Zhang, J. R. Weertman, and J. A. Eastman, *Appl. Phys. Lett.* **87**, 061921 (2005).
- ⁴⁷M. Jin, A. M. Minor, E. A. Stach, and J. W. Morris, *Acta Mater.* **52**, 5381 (2004).
- ⁴⁸D. S. Gianola, S. V. Petegem, M. Legros, S. Brandstetter, H. Van Swygenhoven, and K. J. Hemker, *Acta Mater.* **54**, 2253 (2006).
- ⁴⁹M. Legros, D. S. Gianola, and K. J. Hemker, *Acta Mater.* **56**, 3380 (2008).
- ⁵⁰T. J. Rupert, D. S. Gianola, Y. Gan, and K. J. Hemker, *Science* **326**, 1686 (2009).